Supplemental Information

Transcription activation is enhanced by multivalent interactions independent of liquid-liquid phase separation

Jorge Trojanowski, Lukas Frank, Anne Rademacher, Pranas Grigaitis & Karsten Rippe

Content

Supplemental analysis

FRAP analysis

Comparison of FRAP for widefield and confocal microscopy setup

The widefield microscope FRAP used in our study provides fast data acquisition and imaging is decoupled from bleaching. However, the resolution along the z-axis is not as good as with a confocal microscopy. We thus compared GFP-LacI diffusion and binding to the reporter array in FRAP experiments with the widefield FRAP system to measurements with a Leica SP5

confocal microscope (Leica, Germany) equipped with a 63x Plan-Apochromat immersion objective. The confocal FRAP experiments were conducted using the Leica LAF software and bleaching with the argon laser lines (458 nm, 476 nm, 488 nm, 496 nm). Images of 128x128 pixel with zoom factor 9 corresponding to 194 nm/pixel were recorded at 1400 Hz line frequency resulting in a frame time of 115 ms. For each cell, 70 pre-bleach and 2 bleach frames were recorded with a 1 µm diameter circular bleach region. It was placed on the reporter array ("on spot") or elsewhere in the nucleus but outside nucleoli ("off spot"). Subsequently, 1200 (on spot) or 300 (off spot) post-bleach frames were recorded (**Fig. S4A-C**). Image analysis and parameter estimation were done as for widefield FRAP with the following adaptations: The post-bleach intensity profiles were not fitted individually but averaged, the estimated bleach profile parameters were applied globally to calculate initial conditions and the fitting range of the correction factor *bgRatio* was set to 0.3 to 2.3. A fit of the data to reaction-diffusion model yielded similar values for the two different FRAP setups of D_{eff} = 2.3 µm^2/s and k_{off} = 0.009 s^{-1} (widefield) vs. D_{eff} = 3.3 µm^2/s and k_{off} = 0.010 s^{-1} (confocal) (**Fig. S4B, C**). The widefield curves recovered to higher values in the first seconds and then showed a similar behavior as the confocal FRAP curves but with a lower immobile fraction (widefield: 7.8 %, confocal: 29 %). These differences can be rationalized by the better z-resolution of the confocal setup that reduces the number of freely diffusive molecules observed below and above the reporter array, which do not contribute to a potential immobile fraction. Moreover, shorter FRAP time courses were recorded with the confocal system due to higher imaging related bleaching and out-of-focus translocation of the reporter array. Potentially, this shorter observation time in confocal mode may lead to a higher estimate of the immobile fraction.

Analysis of FRAP images

Intensities in the region of interest were determined automatically using functions of the NSSQ (*1*) and EBImage (*2*) packages in R (*3*) and the bleached nucleus was segmented by local thresholding (**Fig. S4D**). As dCas9-GFP was depleted in the nucleus, images were blurred and the whole cell was segmented for this construct. For on-spot experiments the reporter array was segmented in the first pre-bleach frame using the 98% quantile inside the nucleus. The bleach region was segmented with an image created from the difference of pre-bleach and first post-bleach frame. To correct for chromatin or cell movements the nucleus was tracked, and positions of spot and bleach region mask were shifted accordingly. If automated tracking failed, spot positions were selected manually in every tenth frame and all masks were shifted accordingly. Average intensities were extracted for each time frame in the nucleus, in a ring-shaped area around the nucleus (background intensity), in the spot area and in a ring-shaped area around the spot (local background). The intensity profile around the center of the bleach position was measured as the median intensity of rings starting with a radius of 1 pixel up to a radius of 9 pixels (20x objective) or 40 pixels (100x objective). The pixel size was 0.63 µm (20x objective) or 0.13 µm (100x objective) based on a reflective grid slide of known size. Recovery

curves of profiles and average intensities were subjected to the following normalizations: Background I_{nuc_bg} in a region around the nucleus was subtracted and intensity profiles $I(r,t)$ were normalized to the average nuclear intensity I_{nuc} to account for bleaching of fluorescence signal during the experiment. The intensity of the center position of the first post-bleach frame $I(r=r_{center},t=0)$ was subtracted. The resulting profile was normalized to the average value before bleaching for each profile position r.

$$I_1(r,t) = I(r,t) - I_{nuc\_bg}(t)$$

$$I_{nuc\_norm}(t) = I_{nuc}(t) - I_{nuc\_bg}(t)$$

$$I_2(r,t) = \frac{I_1(r,t)}{I_{nuc\_norm}(t)}$$

$$I_3(r,t) = I_2(r,t) - I_2(r = r_{center}, t = 0)$$

$$I_{norm}(r,t) = \frac{I_3(r,t)}{mean\big(I_3(r,t<0)\big)}$$

For off-spot experiments the average bleach region intensity was calculated from normalized profiles by averaging intensities from the region center to a radius of 3.5 µm weighted by the pixel number in each ring of the profile and leaving out the innermost value. For quantitating the spot intensity, the nuclear background signal was subtracted. Average spot intensities were normalized by dividing them by the average nucleus intensity, subtracting the minimum value in the first post-bleach frame and dividing by the average pre-bleach value.

$$I_{spot,1}(t) = I_{spot}(t) - I_{nuc\_bg}(t)$$

$$I_{nuc\_norm}(t) = I_{nuc}(t) - I_{nuc\_bg}(t)$$

$$I_{spot,2}(t) = \frac{I_{spot,1}(t)}{I_{nuc\_norm}(t)}$$

$$I_{spot,3}(t) = I_{spot,2}(t) - min\left(I_{spot,2}(t)\right)$$

$$I_{spot,norm}(t) = \frac{I_{spot,3}(t)}{mean\left(I_{spot,3}(t<0)\right)}$$

Segmented image series were manually curated by removing cells where (i) segmentation or tracking failed, (ii) the normalized spot intensity exceeded 1.2, (iii) the spot intensity was less than 25% above background, or (iv) the recovery curve displayed strong intensity jumps.

Models for clustered binding sites and diffusion

Recovery of fluorescence intensity inside the spot area was modeled by a localized cluster of binding sites b inside a cylindrical volume of radius r_s that can be bound by freely diffusing particles f to form a complex c according to the theoretical framework established previously (*4*):

$for\ r \leq r_s$:

$$\frac{\partial f(r,t)}{\partial t} = D_{eff} \cdot \nabla_r^2 f(r,t) - k_{on}^* \cdot f(r,t) + k_{off} \cdot c(r,t)$$

$$\frac{\partial c(r,t)}{\partial t} = k_{on}^* \cdot f(r,t) - k_{off} \cdot c(r,t)$$

$for\ r\ > r_s$:

$$\frac{\partial f(r,t)}{\partial t} = D_{eff} \cdot \nabla_r^2 f(r,t)$$

$$c\ =\ 0$$

Here, D_{eff} is the effective diffusion coefficient that includes free diffusion and transient non-specific binding to chromatin. The apparent rate $\mathrm{k}_{\mathrm{on}}^*$ for binding to cluster sites includes the equilibrium concentration of free cluster binding sites. We extended this description by using a bleach region that can be larger than the spot area and modeled the initial conditions by a Gaussian function with a central plateau. It accounts for diffusion during the time between bleaching and the first post-bleach frame.

$$I\big(r < r_p, t = 0\big) = 0$$

$$I\left(r\ \geq r_p, t = 0\right)\ =\ A\ \cdot \left(1 - e^{\frac{-(r-r_p)^2}{\sigma}}\right)$$

In this equation, r_p is the plateau radius, A the intensity of the unbleached peripheral region and σ describes the width of the Gaussian. The binding site cluster was approximated as a cylinder with a homogeneous distribution of binding sites in z-direction at the center of a cylindrically shaped nucleus. This allowed us to formulate the system of partial differential equations in polar coordinates. For the estimation of diffusion coefficients from off-spot FRAP experiments we used a simplified model with only a diffusive and an unspecific immobile fraction.

$$\frac{\partial f(r,t)}{\partial t} = D_{eff} \cdot \nabla_r^2 f(r,t)$$

The time evolution of intensity profiles was simulated by solving the PDE system numerically using the R-package ReacTran (*5*) that implements finite-difference grids. The radial axis from the spot center to the nucleus radius was split into 50 intervals to yield 50 concentric grid cells. A single ring-shaped grid cell was used for each radial interval assuming symmetry around the central spot position. Fluxes at the boundaries were set to zero. The model simulation resulted in radial profiles that were converted to averaged intensity values. The intensity in an area up to a radius of 3.5 µm for the pure diffusion model and from 0.0 to 1.0 µm for the reaction-diffusion model was averaged with the method described above for the image data.

Parameter estimation from recovery curves

We used individual recovery curves from off-spot FRAP measurements to estimate D_{eff} of the ligand constructs. The nuclear radius was determined from the segmented nuclear mask. The initial profile of free diffusible molecules $f(r,t=0)$ was estimated from the normalized profile of the first post-bleach frame fitted by a Gaussian with a plateau diameter of r_p and the parameter σ describing the gaussian width. The amplitude was set to 1. Recovery of the normalized intensity in the bleach region was then fitted by a diffusion-only model with an immobile fraction using the *nls* function in R with multiple start values for the fit parameters. Starting values were varied between D_{eff} = 0.1 and 5 μm^2/s and an immobile fraction f_i = 0.1 and 0.5. The best fit out of all starting values was selected. The median of D_{eff} across single cell recovery curves for each ligand-target combination was used for further analysis. The normalized on-spot recovery curves were used to calculate k_{off} and immobile fraction of molecules at the binding site cluster. The immobile fraction f_i was determined by fitting the data to a single exponential to the mostly binding dominated part of the recovery curve after 30 seconds:

$$I(t|t > 30s) = A + B \cdot \left(1 - e^{-k \cdot t}\right)$$

The immobile fraction was calculated as

$$f_i = 1 - A - B$$

with $f_i \leq 0.5$. The full recovery time course was then fitted with the localized binding site cluster model with D_{eff} and f_i fixed. An approximated start value of the pseudo on-rate k_{on}^* was calculated from the ratio of spot and nucleus intensity before bleaching.

$$spotRatio = \frac{median\left(I_{spot}(t<0) - I_{spot\_bg}(t<0)\right)}{median\left(I_{spot\_bg}(t<0)\right)}$$

In (pre-bleach) equilibrium the ratio of bound and free molecules in the spot is given by

$c/f = k_{on}^*/k_{off}$, so that k_{on}^* can be calculated as

$$k_{on}^* = \frac{c}{f} \cdot k_{off} = spotRatio \cdot k_{off}$$

A correction factor *bgRatio* that is multiplied with *spotRatio* was introduced as a free fit parameter to adjust for differences in the ratio of free and bound fraction. The initial profile $f(r,t=0)$ was estimated as described for the off-spot experiments and $c(r \leq r_s, t=0)$ was set to 0. Model simulations for a given parameter set yielded radial profiles of free and bound molecules *f(r,t)* and *c(r,t)* for each timepoint. These were processed and normalized like the imaging intensities:

$$y_{norm}(r,t) = (1 - f_i) \cdot \frac{f(r,t) + c(r,t)}{f(r, t = 240s) \cdot (1 + spotRatio \cdot bgRatio)}$$

This normalized profile was integrated from the spot center to 1.0 μm yielding a normalized

time course $y_{norm}(t)$ that could be fitted to the data. The recovery curves were fitted by minimizing the sum of squared residual on a grid of parameter values for k_{off} and *bgRatio* as described previously (*4*). First, k_{off} values were varied between 10^{-4} and 0.1 s^{-1} in seven steps and *bgRatio* between 1 and 3.45 in steps of 0.35. The best parameter pair was used as a starting point for a refined optimization. In this second optimization the value of k_{off} was multiplied by a factor between 0.2 and 8 and *bgRatio* was varied in steps of 0.03. The parameter pair with the smallest sum of squared residuals was selected as the best fit.

Model for TF residence time dependent activation

TF residence time becomes functionally relevant if a kinetic proof-reading mechanism (*6*) is present that contains an energy-dissipating step subsequent to DNA binding like nucleosome remodeling (*7*) or posttranslational modifications of the transcription complex or the TF itself (*8*). Such a mechanism in generic form is depicted in **Figure 6H** where the TF binds with rate constant k_{on} to the free promoter (state *A*) and dissociates from the bound state *B* with rate constant k_{off}. An energy dependent step with rate k_1 leads to an activated TF bound state. The modified TF can dissociate from this state with the same dissociation rate constant k_{off} as in state *B*. RNA is produced only from the activated state *C* with rate constant k_t and is degraded with rate k_m. The total concentration of all promoter states is normalized to one, so that $A + B + C = 1$. The concentration of free TF is assumed to be high compared to the concentration of binding sites so that it can be absorbed into a pseudo-binding rate constant $k^*_{\mathrm{on}} = k_{\mathrm{on}} \cdot [TF]$. Furthermore, the loss of free modified TFs is taken to be comparatively fast so that rebinding of modified TFs can be neglected. The model is then described by the following system of ordinary differential equations:

$$\frac{dB}{dt} = k^*_{on} \cdot (1 - B - C) - \left(k_{off} + k_1\right) \cdot B$$

$$\frac{dC}{dt} = k_1 \cdot B - k_{off} \cdot C$$

$$\frac{dR}{dt} = k_t \cdot C - k_m \cdot R$$

The steady state levels are:

$$B = \frac{1}{\left(1 + \frac{k_{off}}{k^*_{on}}\right) \cdot \left(1 + \frac{k_1}{k_{off}}\right)}$$

$$C = \frac{1}{\left(1 + \frac{k_{off}}{k^*_{on}}\right) \cdot \left(1 + \frac{k_{off}}{k_1}\right)}$$

$$R = \frac{k_t}{k_m \cdot \left(1 + \frac{k_{off}}{k_{on}^*}\right) \cdot \left(1 + \frac{k_{off}}{k_1}\right)}$$

The TF concentration can be expressed in units of K_D which leads to the equation for steady state RNA levels plotted in **Fig. 6 H, right**:

$$R = \frac{k_t}{k_m \cdot \left(1 + \frac{1}{[TF]}\right) \cdot \left(1 + \frac{k_{off}}{k_1}\right)}$$

The occupancy θ can be determined from the sum of (normalized) states *B* and *C*:

$$\theta = B + C = \frac{1}{1 + \frac{k_{off}}{k_{on}^*}} = \frac{[TF]}{[TF] + \frac{k_{off}}{k_{on}}}$$

Both steady state RNA levels and binding site occupancy depend on the TF concentration. The RNA levels are limited by the last term of the denominator that contains the ratio of the TF modification rate constant and the dissociation rate. Hence, the residence time $\tau_{res} = 1/k_{off}$ regulates the steady state RNA level. This is illustrated by setting the modification rate constant to k_1 = 0.005 s^{-1} and comparing two different dissociation rates k_{off} = 0.006 s^{-1} (τ_{res} = 167 s) and k_{off} = 0.014 s^{-1} (τ_{res} = 71 s). These k_{off} / τ_{res} values reflect those observed for dCas9-GFP-VPR targeted to the *tet*O sites by mutated and wild type sgRNA. For simplicity the binding behavior was approximated by a weighted average of the apparent residence time and the immobile fraction f_i, that was assumed to have a residence time equal to the FRAP experiment duration (τ_{res} = 240 s).

$$k_{off} = \frac{1}{(1 - f_i) \cdot \tau_{FRAP} + f_i \cdot 240\ s}$$

The promoter becomes saturated at somewhat higher TF concentrations for the higher k_{off} rate as computed for a value of k_{on} = 10^5 M^{-1} s^{-1}, corresponding to K_d = 60 nM and K_d = 140 nM, respectively (**Figure 6H, left**). Notably, the RNA output is not only dependent on binding site occupancy but also directly reflects k_{off}. This is illustrated by the realtion of RNA production and TF concentration given in units of the dissociation constant K_d and thus normalized to the same promoter occupancy (**Figure 6H, right**). It can be seen that transcription increases with τ_{res} and the difference between the higher and lower τ_{res} persists even if full occupancy is reached. Thus, TF residence time and not binding site occupancy governs RNA production at saturating TF expression levels.

Characterization of transcription incompetent BLInCR complexes

The BLInCR-dCas9 and BLInCR-loop complexes with VPR or VP16 were clearly enriched at the reporter array upon light induction (**Fig. S1A**). In addition, when coupled to VPR they efficiently induced BRD4 recruitment and H3K27 acetylation (**Fig. 5D**). Nevertheless, these TF

constructs were unable to induce transcription. While the BLInCR-loop complex with VPR/VP16 is newly introduced here, the BLInCR-dCas9 complex has been used previously to induce expression of selected single-copy genes, although with variable efficiency for the target genes and sgRNAs studied (*9*). Furthermore, the BLInCR-TetR/rTetR complex is a strong transcription activator as shown here and in our previous work (*10*). To further dissect the inability of the BLInCR-dCas9 complex to induce transcription at the reporter array we conducted a number of additional experiments. We tested if the large size of the light-inducible dCas9 complexes (BLInCR-dCas9 VPR, 340 kDa; BLInCR-loop VPR, 348 kDa) hindered transcriptional induction. Accordingly, a fusion complex of comparable size (340 kDa) containing tetrameric GFP as a spacer between dCas9 and VPR (dCas9-GFP4-VPR) was studied (**Fig. S5A**). The GFP4 containing complex was a strong activator although induction of transcription was somewhat reduced as compared to dCas9-GFP-VPR (**Fig. S5A**). In contrast, a direct fusion of dCas9 with the catalytic core domain of the histone acetyl transferase p300 induced targeted H3K27 acetylation and BRD4 recruitment (**Fig. 5D**) but did not activate transcription (**Fig. S5A**). The dCas9-p300 fusion, however, is capable to activate certain single-copy genes (*11*) including the *IL1RN* gene (*12*) that was induced with CIBN-dCas9-CIBN in the above mentioned publication (*9*). Next, we tested if the BLInCR-dCas9 complex can activate a turboRFP reporter gene containing 5 x *tetO* sites upstream of a CMV minimal promoter in HeLa cells (**Fig. S5B**)**.** This HeLa cell line was generated by random stable integration of a plasmid construct containing the silent 5xtetO-miniCMV-turboRFP reporter coupled to a cassette expressing a rTetR-transactivator (rTetR-TA) fusion that binds to the *tetO* sites in presence of doxycycline. Targeting a dCas9 VPR fusion to the *tetO* sites using a suitable sgRNA or recruitment of rTetR-TA by doxycycline efficiently induced the reporter expression after 24 hours (**Fig. S5C**). In contrast, targeting BLInCR-dCas9 with PHR-GFP-VP64 to the reporter as used in ref. (*9*) with a *tet*O sgRNA and blue-light illumination did not lead to turboRFP expression (**Fig. S5C, bottom**). Thus, we conclude that recruitment of the VPR activation domains consistently induces histone acetylation with all DBDs tested. Histone acetylation on its own is sufficient at some genes to subsequently induce transcription. However, the CMV minimal promoter used here appears to additionally require a certain configuration of the AD to initiate transcription that is not provided with BLInCR-dCas9/-loop constructs.

Supplemental figures

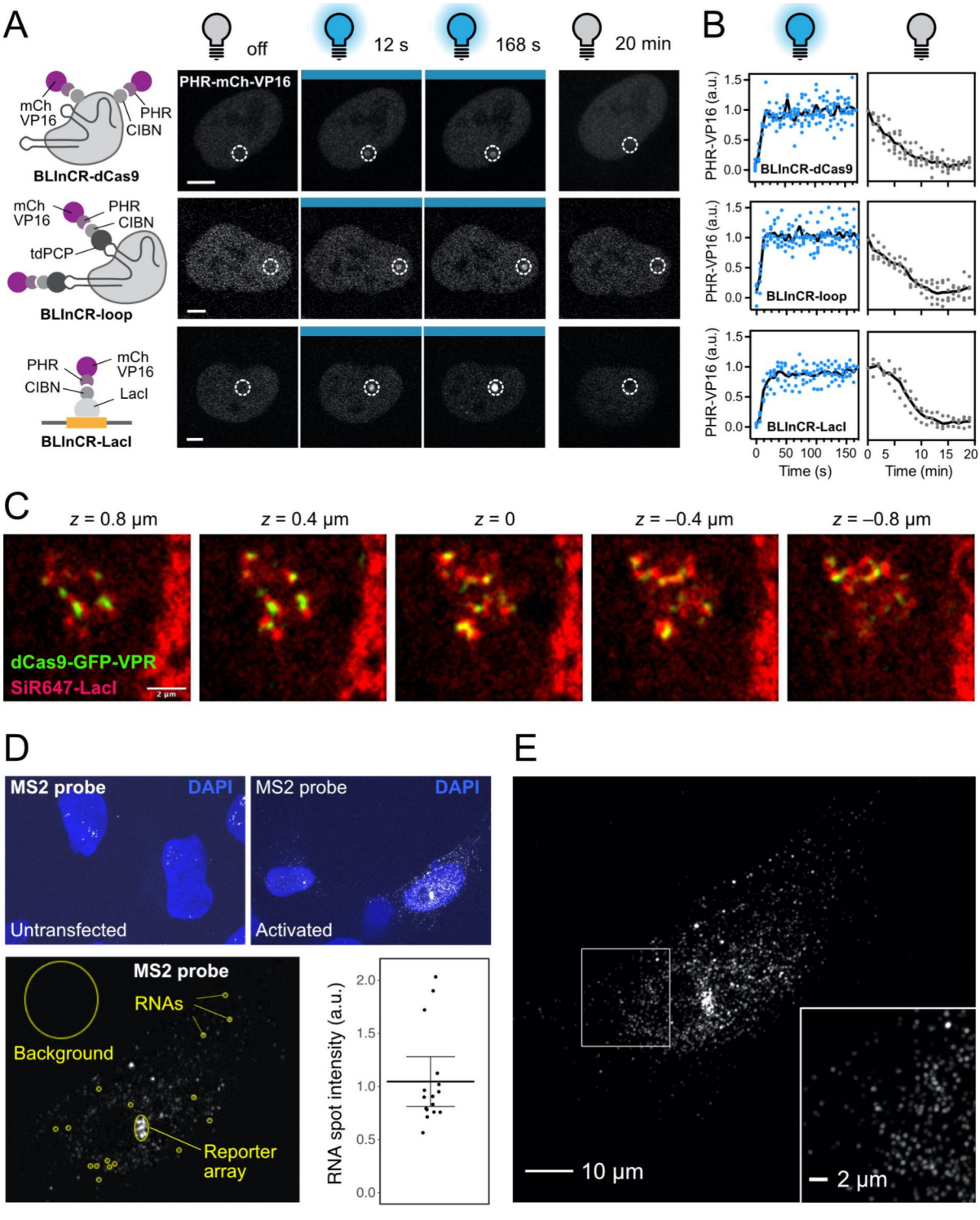

Figure S1. Light induced activator binding and transcription activation

(**A**) Confocal microscopy images of U2OS 2-6-3 cells expressing BLInCR-dCas9, -loop and -LacI complexes depicted in the scheme. These constructs bind the reporter array upon blue light illumination and dissociate if light is switched off. The dashed line circle marks the reporter array, which was identified by a co-transfected TetR-YFP marker (not shown, see **Fig.**

1 D). Scale bars, 5 µm. (**B**) Quantification of the recruitment and dissociation kinetics for the light and dark phase, respectively (*n* = 3 - 5 per construct). Solid line depicts the normalized intensities averaged over all cells for each timepoint. (**C**) SRRF image z-stack of decondensed reporter array in a cell transfected with SiR647-labeled SNAPtag-LacI (red) and dCas9-GFP-VPR (green); distance of z-slices, 0.4 µm; scale bar, 2 µm. (**D**) Single molecule RNA FISH of MS2-reporter RNA in U2OS 2-6-3 cells visualized by confocal microscopy. Top: Comparison of untransfected cells (left) and cells induced by transfection of CIBN-rTetR and PHR-GFP-VP16 and overnight illumination. Bottom: Single z-plane image showing transcripts at the reporter array, in the nucleus and in the cytoplasm. About 80 nascent RNAs were detected as estimated from the intensity of single RNA spots indicated with yellow circles. (**E**) SRRF maximum intensity projection image resolving a total of about ~2000 distinct RNA spots with ~1400 located in the nucleus and ~600 in the cytoplasm.

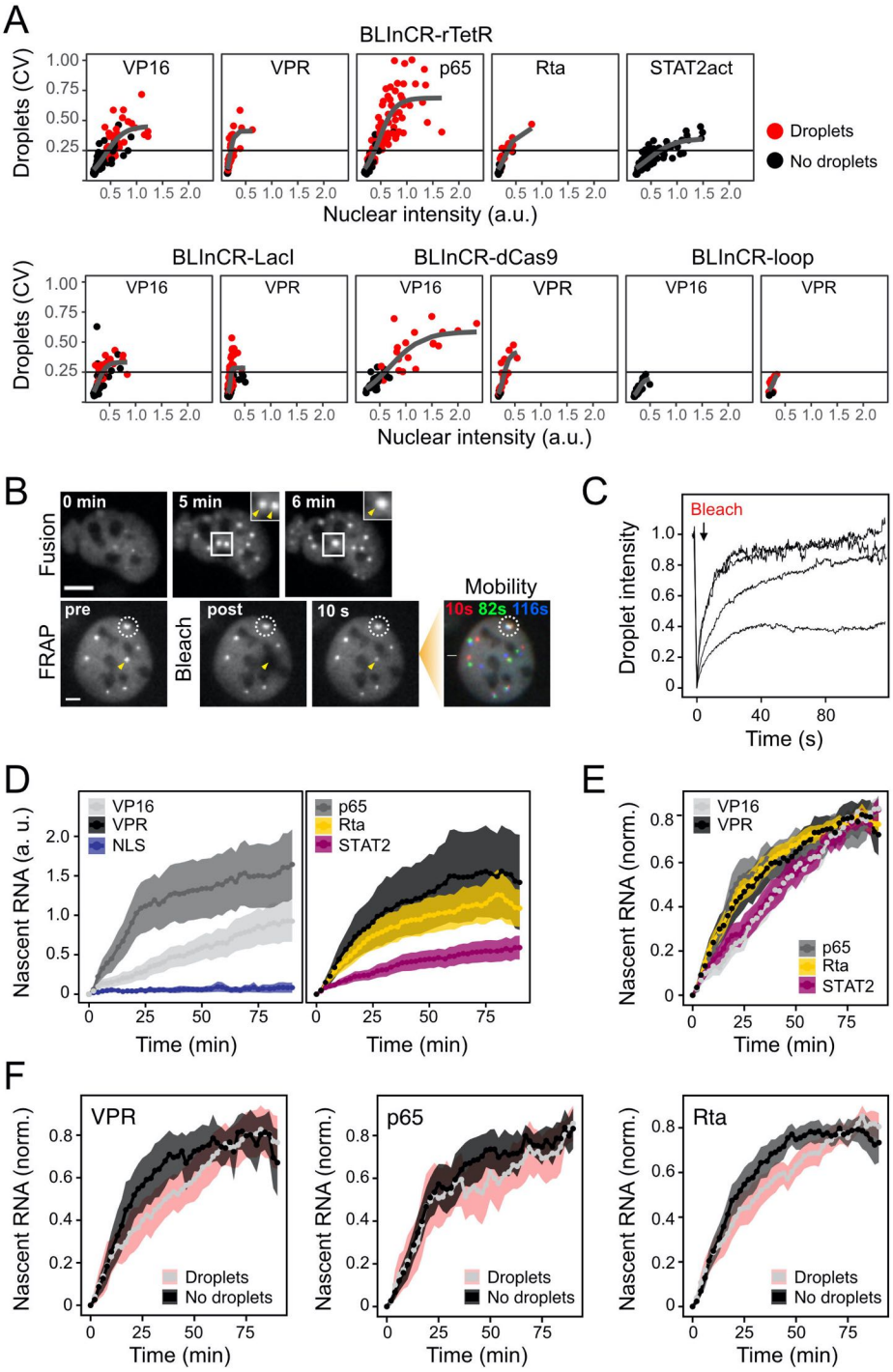

Figure S2. AD droplet formation propensity and transcription activation kinetics

(**A**) Optodroplet formation at different expression levels for the indicated PHR-GFP-AD construct in combination with different targeting complexes carrying a CIBN construct. PHR-GFP-AD fluorescence was measured by microscopy in the nucleus after several cycles of illumination. Droplet abundance was quantitated as the coefficient of variation (CV) of the GFP nuclear signal as well as by manual annotation as droplet containing (red) or not (black) after visual inspection. The critical concentration was determined as the nuclear intensity at which the fitted logistic function (black line) crossed the threshold at 0.25. (**B**) Liquid-like properties

of PHR-GFP-VPR droplets formed outside the reporter array. Top: Image series showing the fusion of two droplets. Bottom: FRAP image series. Droplets were highly dynamic and recovered within seconds after bleaching (yellow arrow). The droplets also showed displacement from their original position as apparent from their color-coded positions after 10, 82 and 116 s. The reporter array is marked by a dashed circle. Scale bars 5 μm. (**C**) FRAP recovery curves of PHR-GFP-VPR optodroplets displaying predominantly fast recovery. (**D**) Averaged transcription activation kinetics of combined responder and non-responder cells (*n* = 37-132 cells per condition). Ribbon, 95 % CI. (**E**) Averaged transcription activation kinetics after normalization to the maximum value of individual trajectories only for responding cells where nascent RNA was detectable. Ribbon, 95% CI. (**F**) Same as panel E for VPR, p65 and Rta but after dividing the cells into a group that displayed droplet formation outside the array and another that did not. Droplet formation due to an increased nuclear concentration of the activator did not enhance transcription activation kinetics. Ribbon, 95% CI; n= 13-40 cells per condition.

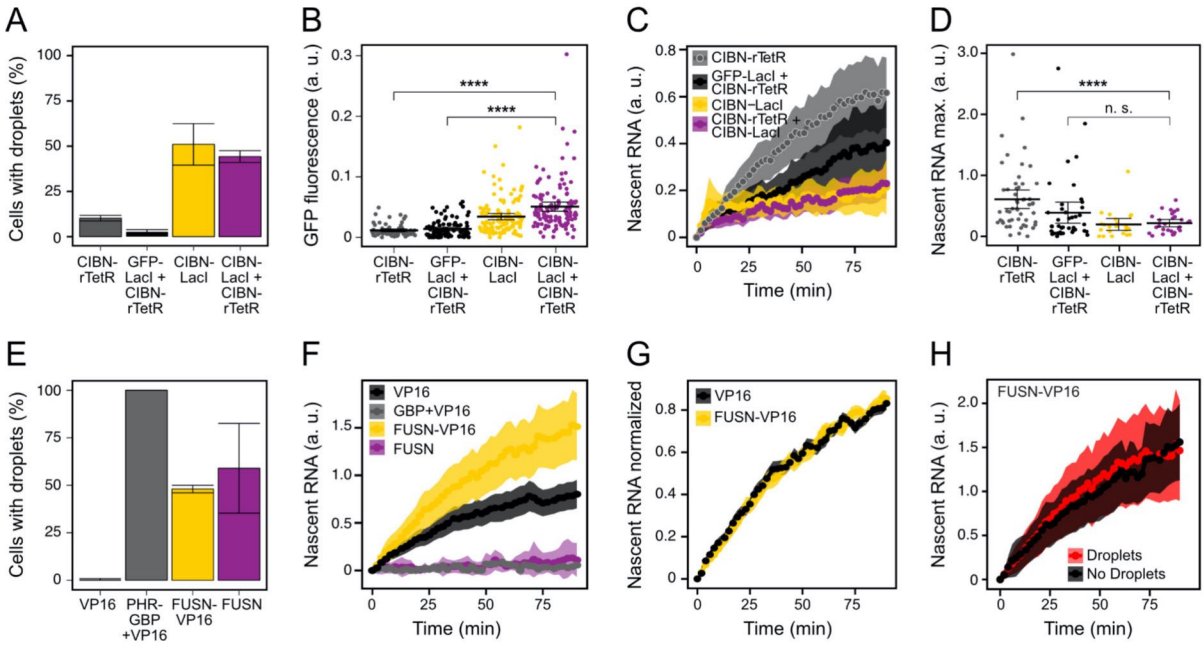

Figure S3. Effect of droplet formation on transcription activation by VP16

Transcription activation of PHR-GFP-VP16 upon light induction was studied in dependence of factors that affected droplet formation of this activator construct. (**A**) Fraction of cells containing visible optodroplets; bar: mean, error bars: min. and max. of 2 replicate experiments. The presence of CIBN-LacI promoted droplet formation. (**B**) GFP signal at the reporter array. In the presence of CIBN-LacI additional PHR-GFP-VP16 molecules were recruited. Dots: single cell values, bar: mean, error bars: 95% CI. ****: $p < 0.0001$, two-sided Welch's t-test. (**C**) Average nascent RNA production time courses for responding cells. Addition of CIBN-LacI reduced transcription activation. Ribbon: 95% CI. **(D)** Nascent RNA plateau levels of responding cells. CIBN-LacI had a repressive effect. Dots: single cell values, bar: mean, error bars: 95% CI. n.s.: not significant, ****: $p < 0.0001$, two-sided Welch's t-test. **(E)** Fraction of cells displaying optodroplets. A fusion with FUSN or addition of PHR-GBP to bind an additional PHR domain enhanced droplet formation; bar: mean, error bars: min. and max. of 2 replicate experiments. **(F)** Average nascent RNA production time courses for responding cells. Ribbon: 95% CI. Note that only a few cells show transcription for PHR-GBP+VP16 and for FUSN. It can be seen that the FUSN-VP16 fusion enhanced transcription activation by VP16. (n = 94-134) **(G)** Average normalized time courses of nascent RNA for responder cells normalized to maximum value of individual trajectories to visualize dynamics. Transcription activation kinetics are not affected by the FUSN fusion. Ribbon, 95% CI. (**H)** Average time courses of nascent RNA production for responder cells activated by FUSN-VP16 divided into groups with or without visible optodroplets. No differences in activation kinetics and maximum levels between the two groups were apparent. Ribbon, 95% CI; n = 47 cells per condition.

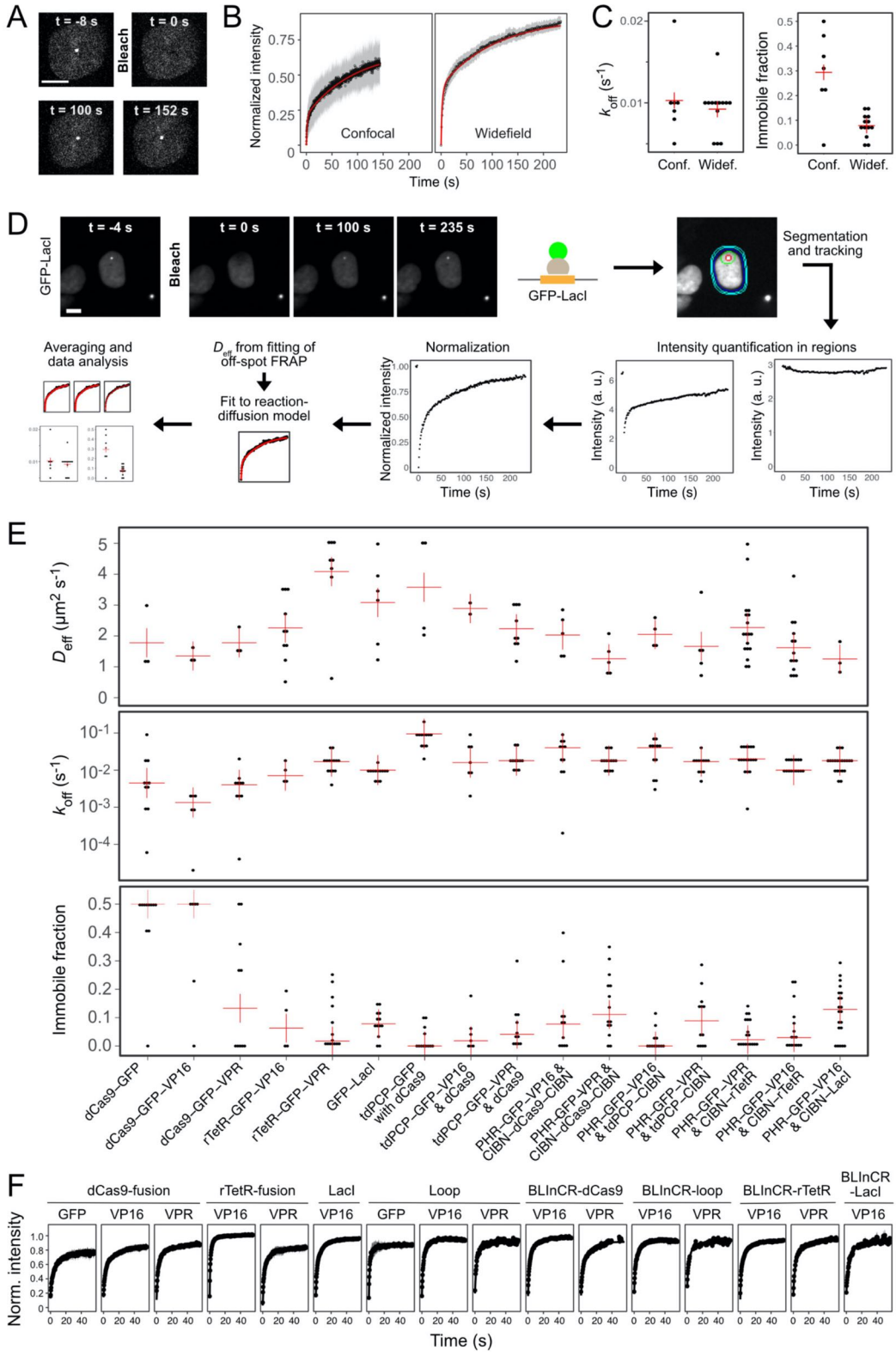

Figure S4. Experimental FRAP setup and data analysis

(**A**) Image series of confocal FRAP of GFP-LacI bound to the reporter array. Scale bar: 10 µm. (**B**) Average recovery curves of GFP-LacI obtained by confocal and widefield FRAP. Ribbon, 95 % CI; red line, fit of data to a reaction-diffusion model. The diffusive fraction is larger for widefield FRAP as discussed above in the Supplemental Methods section. (**C**) Binding

parameters of GFP-LacI fits in confocal (Conf.) and widefield (Widef.) mode. Red cross: median. (**D**) Image analysis workflow for widefield FRAP illustrated for GFP-LacI as an example (scale bar 10 µm). Automated segmentation of spot (red), local background region (green), nucleus (blue) and background around nucleus (cyan) over the time course is followed by intensity quantification in these regions. The spot intensity was normalized, and binding parameters were obtained by fitting a reaction-diffusion model, which uses the effective diffusion coefficient determined in off-spot FRAP experiments. Normalized data, fit curves and fit parameters of single cells were averaged. (**E**) Distribution of parameters estimated from single cell recovery curves by a reaction-diffusion model. Effective diffusion coefficients were determined from off-spot FRAP while dissociation rate and immobile fraction were measured at the array. Red cross: median. Dots: single cell values. (**F**) Average recovery curves for off-spot FRAP to determine the diffusion behavior of activation complexes. Fits of the data to a diffusion model are shown as solid line.

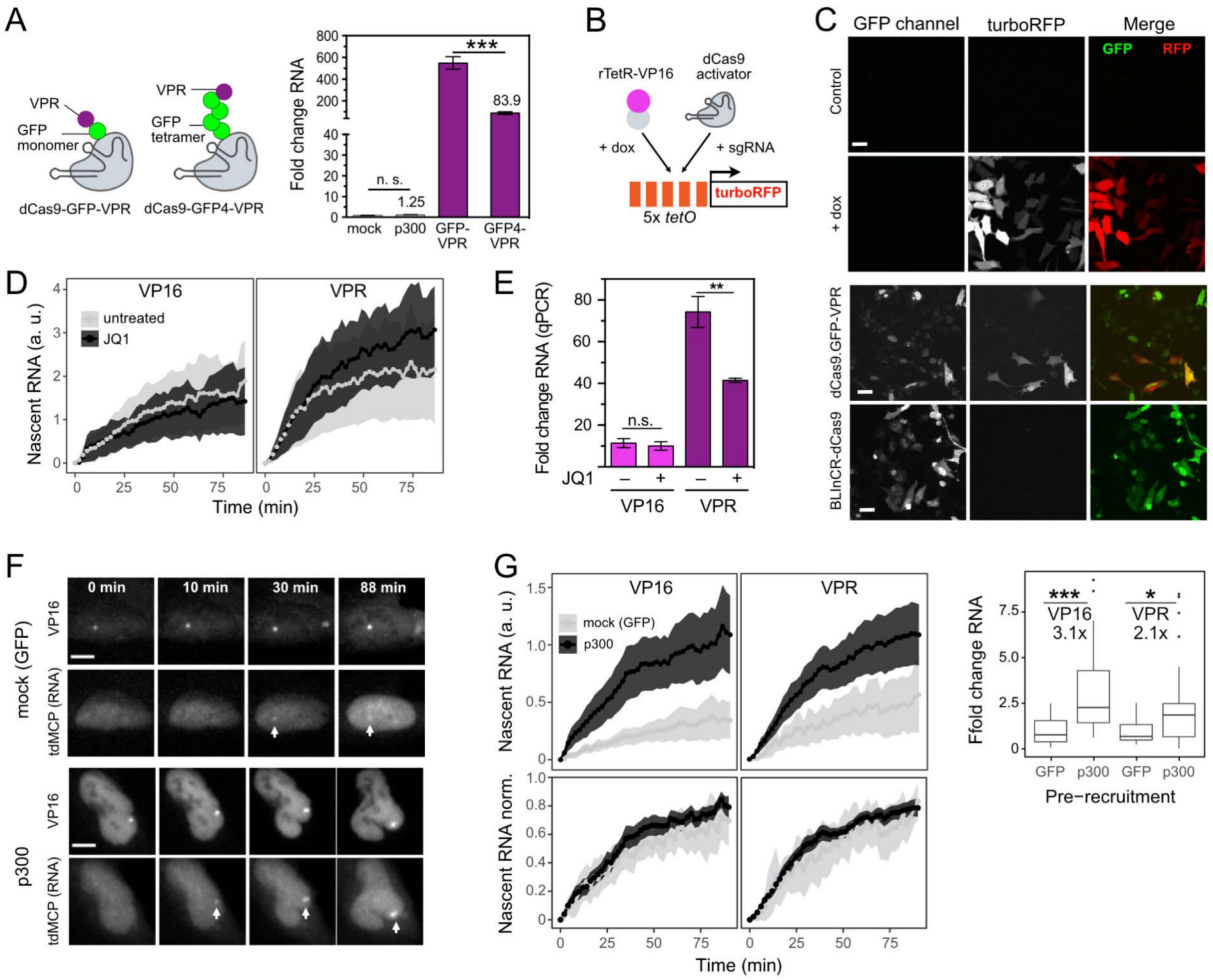

Figure S5. Histone acetylation, BRD4 binding and transcription activation

(**A**) Comparison of transcription induction measured by qRT-PCR of a dCas9-GFP4-VPR complex with a tetrameric GFP spacer and dCas9-GFP-VPR as a reference with the data from **Fig. 5A**. Data are mean fold changes and standard deviation (*n* = 3) of reporter RNA induction levels normalized to actin mRNA and relative to mock; n. s., $p > 0.05$; ***, $p < 0.001$; two-sided unpaired Student's t-test. (**B**) Experimental strategy for testing the activation potential of the BLInCR-dCas9 complex in the HeLa 5 x *tetO*-miniCMV-turboRFP reporter cell line. The reporter turboRFP protein was induced by either addition of doxycycline to bind rTetR-VP16 at the *tetO* promoter sites or by targeting a dCas9 activator complex with sgRNA to this locus. (**C**) Representative fluorescence microscopy images of turboRFP reporter signal after 24 h induced by rTetR-VP16 or transient transfection with a *tet*O sgRNA and dCas9-GFP-VPR or the BLInCR-dCas9 complex (CIBN-dCas9-CIBN + PHR-GFP-VP64) (*9*) and light illumination. While dCas9-GFP-VPR induced some transcription albeit at lower levels than rTetR-VP16, the BLInCR-dCas9 failed to do so. Scale bar: 20 μm. (**D**) Averaged time course data of light-induced nascent RNA production using PHR-GFP-VP16/-VPR and CIBN-rTetR (BLInCR-rTetR) for untreated cells or cells pre-treated with JQ1 at 1 μM concentration for 3 h (*n* = 7-20 cells per condition). Mean intensities with upper and lower boundaries corresponding to the 95% CI are shown. (**E**) Bulk reporter RNA levels measured by qRT-PCR for the conditions

depicted in panel D at the 90 min endpoint of the time course. Data are fold changes in reporter RNA induction levels normalized to actin mRNA and relative to mock ± s.d. (n = 3); ns, p > 0.05; **, p < 0.01 two-sided unpaired Student's t-test. (**F**) Representative widefield live cell images of time-resolved nascent RNA production (tdMCP-tdTomato) upon light-induced VP16 recruitment to CIBN-rTetR. Cells either had dCas9-GFP ("mock") or dCas-GFP-p300core ("p300") pre-recruited to the *lacO* sites of the reporter before induction. Arrows indicate nascent RNA enriched at the reporter array. Scale bars, 10 µm. (**G**) Quantification of nascent RNA kinetics for the experimental setup described for panel F for VP16 and VPR (n = 9-54 cells per condition). Pre-recruitment of p300 led to a 3.1-fold (VP16) or 2.1-fold (VPR) higher production of nascent RNA as shown in the box plot. Intensity values were normalized to the mean value of the respective mock pre-recruitment. *, p < 0.05; ***, p < 0.001; two-sided Welch's t-test. Bottom: Nascent RNA time courses normalized to their maximum show no effect of p300 pre-recruitment on the kinetics of the activation process.

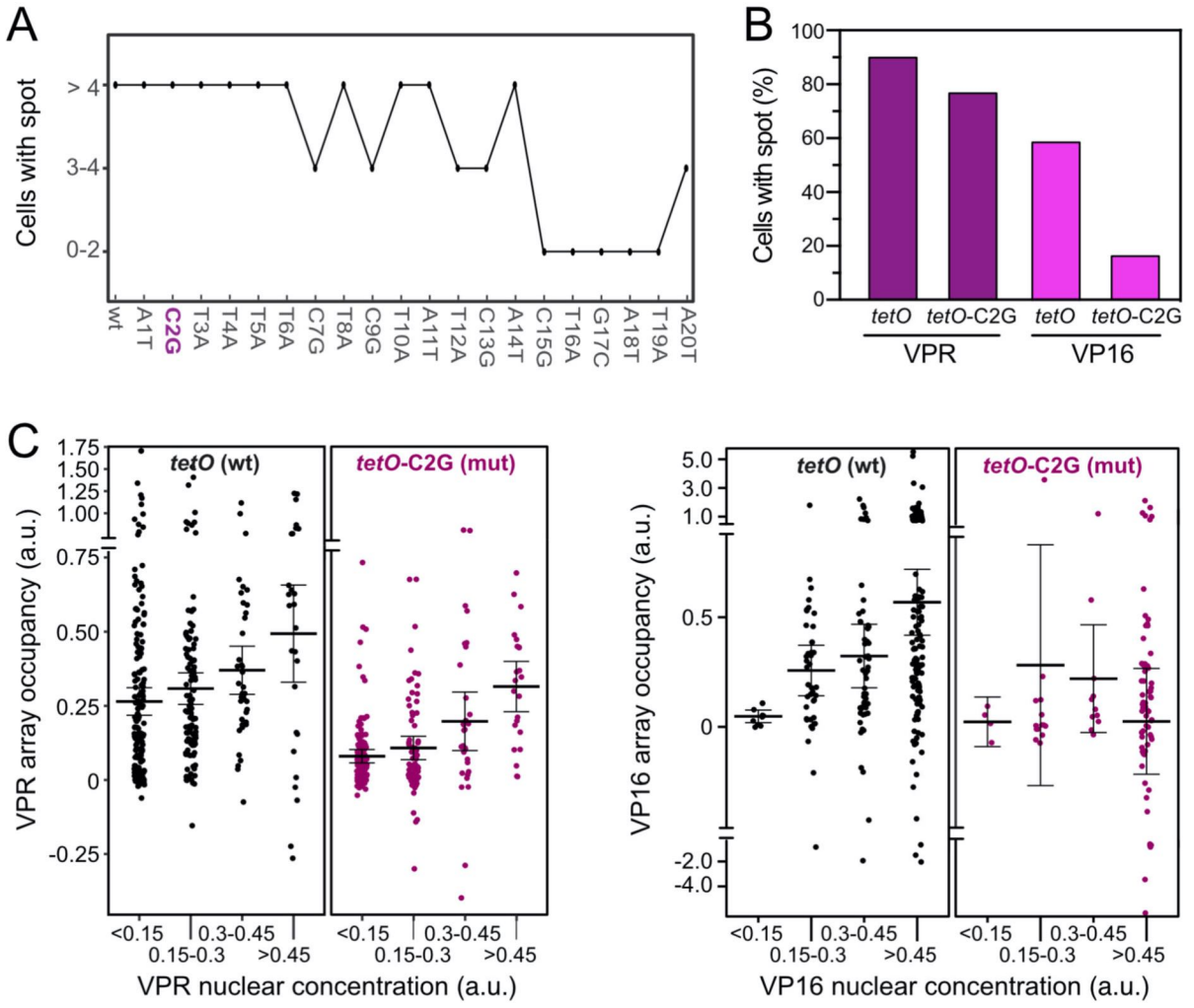

Figure S6. Modulation of residence time via sgRNA mutations

(**A**) Screen of *tetO*-sgRNA mutations that reduced dCas9 binding to *tet*O sites but still enrich at the reporter array. The mutations introduced into the sgRNA targeting region are depicted on the x-axis. dCas9-GFP-VPR was recruited to the reporter with a given sgRNA and the number of cells with visible reporter spot recruitment (GFP) was counted per field of view. (**B**) Fraction of cells with visible reporter array spots for dCas9-GFP-VPR or dCas9-GFP-VP16 recruited with the wildtype (*tet*O) or the mutated (*tet*O-C2G) sgRNA. A total of n = 127-175 cells were evaluated per condition. (**C**) Reporter array occupancy in dependence of nuclear concentration of dCas9-GFP-VPR or dCas9-GFP-VP16 for sgRNA-wt and sgRNA-mut. Concentrations were determined from nuclear fluorescence intensities of dCas9-GFP-VPR/-VP16 and cells were grouped according to this concentration. Occupancy corresponds to the GFP array intensity above background normalized to the co-transfected tagBFP-LacI array marker. Dots correspond to individual cells; mean and 95% CI error bars are indicated. Note the axis break to visualize the majority of cells and outliers in one plot.

Supplemental Tables

Table S1. Plasmid constructs

Plasmid	Comment	Reference
DNA binder		
rTetR-GFP	Contains same NLS as VP16 constructs	This study
rTetR-GFP-VP16		This study
rTetR-GFP-VPR		This study
CIBN-rTetR	Contains T2A-Puro resistance marker	This study
GFP-LacI		(*13*)
CIBN-LacI		(*10*), Addgene #103814
SNAPtag-LacI	LacI in pSNAPf vector (New England Biolabs)	This study
dCas9	dCas9 coding region from Addgene #60910, contains HA-tag	This study
dCas9-GFP		(*14, 15*)
dCas9-GFP-VP16		This study
dCas9-GFP-VPR		(*14, 15*)
dCas9-GFP_4-VPR		This study
dCas9-GFP-p300	p300 core domain from Addgene #61357	This study
CIBN-dCas9-CIBN		(*9*), Addgene #60553
PHR constructs		
PHR-GFP	Contains same NLS as VP16 constructs	(*10*)
PHR-GFP-VP16	VP16 domain from ref. (*16*)	This study
PHR-GFP-VPR	VPR domain from Addgene #63798	This study
PHR-GFP-p65	p65 domain from Addgene #63798	This study
PHR-GFP-Rta	Rta domain from Addgene #63798	This study
PHR-GFP-STAT2	STAT2 activation domain from ref. (*17*)	This study
PHR-GFP-FUSN	FUSN from ref. (*18*), Addgene #122148	This study
PHR-GFP-FUSN-VP16	FUSN from ref. (*18*), Addgene #122148	This study
PHR-GBP	GBP from ref. (*19*)	This study
Other constructs		
tdPCP-GFP	Tandem PCP from Addgene #40650	This study
tdPCP-GFP-VP16	TATA-box of the promoter removed	This study
tdPCP-GFP-VPR	TATA-box of the promoter removed	This study
tdPCP-CIBN	TATA-box of the promoter removed	This study
tdMCP-tdTomato	From Addgene #40649 and #54642 with TATA-box of the promoter removed	This study
mCherry-BRD4	Murine BRD4 from ref. (*20*)	This study

Table S2. sgRNAs sequences used for dCas9 targeting

sgRNA	Targeting sequence (5'-3')
tetO-2xPP7 (wt)	GACTTTTCTCTATCACTGATA
tetO-2xPP7-A1T	GTCTTTTCTCTATCACTGATA
tetO-2xPP7-C2G	GAGTTTTCTCTATCACTGATA
tetO-2xPP7-T3A	GACATTTCTCTATCACTGATA
tetO-2xPP7-T4A	GACTATTCTCTATCACTGATA
tetO-2xPP7-T5A	GACTTATCTCTATCACTGATA
tetO-2xPP7-T6A	GACTTTACTCTATCACTGATA
tetO-2xPP7-C7G	GACTTTTGTCTATCACTGATA
tetO-2xPP7-T8A	GACTTTTCACTATCACTGATA
tetO-2xPP7-C9G	GACTTTTCTGTATCACTGATA
tetO-2xPP7-T10A	GACTTTTCTCAATCACTGATA
tetO-2xPP7-A11T	GACTTTTCTCTTTCACTGATA
tetO-2xPP7-T12A	GACTTTTCTCTAACACTGATA
tetO-2xPP7-C13G	GACTTTTCTCTATGACTGATA
tetO-2xPP7-A14T	GACTTTTCTCTATCTCTGATA
tetO-2xPP7-C15G	GACTTTTCTCTATCAGTGATA
tetO-2xPP7-T16A	GACTTTTCTCTATCACAGATA
tetO-2xPP7-G17C	GACTTTTCTCTATCACTCATA
tetO-2xPP7-A18T	GACTTTTCTCTATCACTGTTA
tetO-2xPP7-T19A	GACTTTTCTCTATCACTGAAA
tetO-2xPP7-A20T	GACTTTTCTCTATCACTGATT
lacO-2xPP7 (wt)	GTCCGCTCACAATTCCACATG

All sgRNAs were cloned into the U6 promoter-driven sgRNA expression vector originally derived from Addgene #61424 and engineered to contain two PP7 stem loops PP7. The PP7 loop sequence was adapted from ref. (*21*).

Table S3. Propensity of the activation domain to form optodroplets

PHR-GFP-AD	DNA binder	Cell number	Droplets (%)	I_{crit} (a. u.) [a]
VP16	CIBN-rTetR	122	27	0.45
VPR	CIBN-rTetR	35	89	0.22
p65	CIBN-rTetR	123	71	0.38
Rta	CIBN-rTetR	34	41	0.36
STAT2	CIBN-rTetR	97	0	0.70
VP16	CIBN-dCas9-CIBN	49	39	0.64
VPR	CIBN-dCas9-CIBN	35	60	0.30
VP16	dCas9 + tdPCP-CIBN	41	0	n. d. [b]
VPR	dCas9 + tdPCP-CIBN	15	80	n. d. [b]
VP16	CIBN-LacI	73	32	0.38
VPR	CIBN-LacI	101	64	0.25

Cells were classified as positive for droplet formation if they displayed nuclear optodroplets in microscopy images in addition to the signal at the reporter array (**Fig. 1E**).

[a] The critical value for droplet formation I_{crit} was determined from the relation of nuclear PHR-GFP-AD concentration and droplet abundance shown in **Fig. S2 A**.

[b] If droplet abundance did not exceed the threshold value within the measured nuclear concentrations the critical value was not determined.

Table S4. Transcription activation kinetics

PHR-GFP-AD	Condition	Cell number	Responders (%)	$t_{1/2}$ (min) [a]	Maximum RNA value (a. u.) [a]
VP16	All cells	64	67	42 (37-46)	1.2 (0.89-1.6)
VPR	All cells	37	84	28 (23-33)	1.7 (1.1-2.4)
VPR	Cells without droplets	15	87	25 (17-34)	1.1 (0.83-1.4)
VPR	Cell with droplets	22	82	30 (24-36)	2.2 (1.0-3.3)
p65	All cells	52	67	26 (21-31)	2.1 (1.6-2.6)
p65	Cells without droplets	23	78	26 (19-33)	2.3 (1.5-3.0)
p65	Cell with droplets	29	59	26 (18-34)	1.9 (1.2-2.7)
Rta	All cells	77	92	28 (25-31)	1.2 (0.92-1.5)
Rta	Cells without droplets	33	94	25 (21-29)	1.2 (0.73-1.7)
Rta	Cell with droplets	44	91	31 (26-36)	1.2 (0.85-1.6)
STAT2	All cells	132	42	38 (34-43)	0.95 (0.66-1.2)
Droplet induction experiments					
VP16	No additional factors	74	70	35 (30-39)	0.61 (0.46-0.76)
VP16	GFP-LacI	97	42	34 (28-39)	0.39 (0.22-0.56)
VP16	CIBN-LacI	118	24	31 (23-38)	0.22 (0.16-0.28)
VP16	CIBN-LacI but no CIBN-rTetR	126	18	20 (13-28)	0.20 (0.09-0.29)
VP16	No additional factors	154	84	34 (31-36)	0.78 (0.63-0.93)
VP16	PHR-GBP	24	4	n. d. [b]	n. d. [b]
FUS-VP16	No additional factors	108	87	37 (34-41)	1.5 (1.1-1.8)
FUS	No additional factors	57	5	n. d. [b]	n. d. [b]

The RNA production at the reporter gene cluster was followed over time via the tdMCP-tdTomato signal. CIBN-rTetR was used as the DNA-binding modules unless stated otherwise.

[a] The maximum of RNA produced was determined from the last five time points at the plateau of the single cell time course, and the time $t_{1/2}$ was determined where half of this values was reached. Mean values and 95%-confidence intervals were calculated from the analysis of responding cells that showed an RNA signal at the reporter array. Data for VP16 and p65 as well as for VPR, Rta and STAT2 were acquired together. A direct comparison of VPR and VP16 done in other experiments yielded a VPR/VP16 ratio of maximum activation values of ~1.5.

[b] Values could not be determined due to the low number of responder cells.

Table S5. FRAP parameters of TF dynamics

Protein(s)	DNA	Residence time (s) [a]	Immobile fraction (%)	D_{eff} ($\mu m^2/s$)	*n*
GFP-LacI	*lacO*	108 (91-134)	8 (5-11)	2.3 (1.5-3.0)	13
GFP-LacI (confocal)	*lacO*	97 (69-167)	29 (14-45)	3.3 (2.0-4.5)	7
dCas9-GFP	*lacO*	74 (32->240)	44 (34-54)	1.8 (0-4.3)	11
dCas9-GFP-VP16	*lacO*	>240 (>240)	37 (15-59)	1.4 (0.8-2.0)	6
dCas9-GFP-VPR	*lacO*	204 (112->240)	19 (4-34)	1.8 (0.7-2.9)	10
dCas9-GFP-VPR	*tetO*	124 (75->240)	36 (25-47)	0.6 (0.4-0.9)	10
dCas9-GFP-VPR	*tetO*-C2G	57 (34-184)	7 (0-16)	- [a]	7
rTetR-GFP-VP16	*tetO*	132 (74->240)	5 (0-14)	4.3 (3.0-5.4)	6
rTetR-GFP-VPR	*tetO*	57 (42-86)	7 (2-12)	3.1 (1.6-4.5)	14
dCas9 + tdPCP-GFP	*lacO*	12 (9-18)	3 (0-5)	3.4 (0.9-6.2)	12
dCas9 + tdPCP-GFP-VP16	*lacO*	33 (17->240)	4 (0-10)	2.9 (0.6-5.2)	7
dCas9 + tdPCP-GFP-VPR	*lacO*	47 (33-83)	7 (1-13)	2.2 (1.7-2.8)	11
CIBN-dCas9-CIBN + PHR-GFP-VP16	*lacO*	28 (18-58)	10 (1-19)	2.0 (1.2-2.9)	11
CIBN-dCas9-CIBN + PHR-GFP-VPR	*lacO*	49 (37-72)	14 (8-21)	1.3 (0.6-1.9)	14
tdPCP-CIBN + dCas9 PHR-GFP-VP16	*lacO*	29 (20-53)	2 (0-4)	2.1 (1.4-2.8)	12
tdPCP-CIBN + dCas9 PHR-GFP-VPR	*lacO*	60 (45-91)	10 (3-16)	1.7 (0.4-3.0)	12
CIBN-rTetR + PHR-GFP-VP16	*tetO*	42 (33-58)	4 (2-7)	2.3 (1.7-2.8)	18
CIBN-rTetR + PHR-GFP-VPR	*tetO*	71 (60-88)	6 (2-10)	1.6 (1.1-2.1)	16

Measurements were conducted with the FRAP widefield microscopy setup except for the indicated measurement of GFP-LacI on a confocal microscopy. Mean values and 95% confidence intervals given in brackets of parameters were determined as described in the Supplemental Methods section.

[a] Not determined. For fitting of the diffusion-binding model the effective diffusion coefficient for dCas9-GFP-VPR with *tetO*-sgRNA(wt) was used.

Table S6. Reporter RNA expression measured by qRT-PCR

DNA binder	AD	Treatment	RNA fold-change
– (mock transfection, reference for normalization)	–	24 h light	1.0
– (untransfected)	–	24 h light	0.9
dCas9-GFP-VP16	VP16 (fusion)	24 h light	6.4
dCas9-GFP-VPR	VPR (fusion)	24 h light	550
dCas9-GFP_4-VPR	VPR (fusion)	24 h light	84
dCas9-GFP-VP16 (tetO-C2G)	VP16 (fusion)	24 h light	0.9
dCas9-GFP-VPR (tetO-C2G)	VPR (fusion)	24 h light	31
dCas9-GFP-p300	p300 (fusion)	24 h light	1.3
rTetR-GFP-VP16	VP16 (fusion)	24 h light + dox	35
rTetR-GFP-VPR	VPR (fusion)	24 h light + dox	217
dCas9 (tetO-PP7)	tdPCP-GFP-VP16	24 h light	4.0
dCas9 (tetO-PP7)	tdPCP-GFP-VPR	24 h light	490
CIBN-dCas9-CIBN	PHR-GFP-VP16	24 h light	1.7
CIBN-dCas9-CIBN	PHR-GFP-VPR	24 h light	1.8
CIBN-dCas9-CIBN	PHR-GFP-VP16	dark	1.3
CIBN-dCas9-CIBN	PHR-GFP-VPR	dark	1.6
dCas9 + tdPCP-CIBN	PHR-GFP-VP16	24 h light	1.0
dCas9 + tdPCP-CIBN	PHR-GFP-VPR	24 h light	1.4
CIBN-rTetR	PHR-GFP-VP16	dox, 24 h light	32
CIBN-rTetR	PHR-GFP-VPR	dox, 24 h light	17.5
CIBN-rTetR + CIBN-LacI	PHR-GFP-VP16	dox, 90 min light	3.1
CIBN-rTetR + GFP-LacI	PHR-GFP-VP16	dox, 90 min light	5.3
CIBN-LacI	PHR-GFP-VP16	dox, 90 min light	1.7
CIBN-rTetR	PHR-GFP-VP16	dox, 90 min light	7.0
CIBN-rTetR	PHR-GFP-FUSN	dox, 90 min light	1.8
CIBN-rTetR	PHR-GFP-FUSN-VP16	dox, 90 min light	70
CIBN-rTetR	PHR-GFP-VP16 + PHR-GBP	dox, 90 min light	1.9
CIBN-rTetR [a]	PHR-GFP-VP16	dox, untreated, 90 min light	11
CIBN-rTetR [a]	PHR-GFP-VPR	dox, untreated, 90 min light	74
CIBN-rTetR [b]	PHR-GFP-VP16	dox, 3 h JQ1, 90 min light	10
CIBN-rTetR [b]	PHR-GFP-VPR	dox, 3 h JQ1, 90 min light	41
CIBN-rTetR [c]	PHR-GFP-VP16	dCas9-GFP *lacO*, dox, 90 min light	9.7
CIBN-rTetR [c]	PHR-GFP-VPR	dCas9-GFP *lacO*, dox, 90 min light	111
CIBN-rTetR [c]	PHR-GFP-VP16	dCas9-GFP-p300 *lacO* + dox, 90 min light	15
CIBN-rTetR [c]	PHR-GFP-VPR	dCas9-GFP-p300 *lacO* + dox, 90 min light	95

Doxycycline was added after transfection for 24 h and cells were illuminated with light for the indicated times. RNA levels were normalized to beta actin mRNA for each sample and fold-changes were determined from the average of three measurements relative to the mock transfected cells.

[a] Reference for the JQ1 pre-treatment experiment.

[b] Cells were pretreated with JQ1 at a 1 μM concentration in the dark for 3 h after doxycycline induction and then activated with light.

[c] Histone hyperacetylation was induced by recruiting dCas9-GFP-p300 with the *lacO* sgRNA for 24 h.

Table S7. Histone acetylation, BRD4 binding and transcription activation

DNA binder and readout	PHR-GFP-AD	Condition	Cell number	Responders (%)	$t_{1/2}$ (min) [a]	Maximum value (a. u.) [a]
dCas9 + tdPCP-CIBN, mCherry-BRD4	VP16	–	37	27	13 (7-20)	0.007 (0.005-0.010)
		JQ1	85	0	–	0.002 (0.002-0.003)
	VPR	–	13	92	13 (8-18)	0.024 (0.016-0.032)
		JQ1	10	10	–	0.005 (0.002-0.008)
CIBN-rTetR, tdMCP-tdTomato (RNA)	VP16	–	29	69	35 (30-39)	1.7 (0.91-2.5)
		JQ1	12	58	28 (18-39)	1.4 (0.63-2.2)
	VPR	–	15	87	29 (20-39)	2.1 (1.0-3.2)
		JQ1	21	81	33 (27-38)	3.0 (2.0-4.0)
	VP16	dCas9-GFP	52	25	35 (25-44)	0.35 (0.18-0.51)
		dCas9-GFP-p300	49	53	31 (27-36)	1.1 (0.76-1.4)
	VPR	dCas9-GFP	27	33	37 (19-54)	0.51 (0.23-0.79)
		dCas9-GFP-p300	72	75	31 (27-34)	1.1 (0.82-1.4)

Transcription activation time course parameters were determined as described for **Table S4**.

[a] Maximum values for RNA production can be compared directly only for the same DNA binding module and experimental conditions. For the experiments with BRD4, values are given for the whole population of responding and non-responding cells due to the low number of responding cells detected after JQ1 treatment.

Table S8. Binding site occupancy of dCas9

DNA binder	AD	sgRNA	Occupancy [a]	Number of cells	Visible array (%) [b]
dCas9	tdPCP-GFP-VP16	*tetO*-2xPP7 (wt)	0.53 (0.41-0.66)	166	78
dCas9	tdPCP-GFP-VPR	*tetO*-2xPP7 (wt)	0.99 (0.77-1.22)	164	93
dCas9-GFP-VP16	VP16 (fusion)	*tetO*-2xPP7 (wt)	0.24 (0.17-0.30)	138	59
		tetO-2xPP7-C2G (mut)	0.03 (0.01-0.06)	127	17
dCas9-GFP-VPR	VPR (fusion)	*tetO*-2xPP7 (wt)	0.32 (0.26-0.37)	175	90
		tetO-2xPP7-C2G (mut)	0.12 (0.09-0.14)	163	76

Binding site occupancy at the reporter array were determined as the ratio of the GFP fluorescence of the activator complex and the blue fluorescence signal of tagBFP-LacI as an array marker.

[a] Mean value and 95% confidence interval measured. Data can be directly compared only for experiments conducted with the same DNA binding module.

[b] Fraction of cells that had the activator complex GFP signal enriched at the site of the array marked by tagBFP-LacI.

Supplemental references

1. J. Trojanowski, A. Rademacher, F. Erdel, K. Rippe, in *Imaging Gene Expression: Methods and Protocols, Methods in Molecular Biology, vol. 2028,* Y. Shav-Tal, Ed. (Springer Nature, New York, 2019), pp. 251-270.
2. G. Pau, F. Fuchs, O. Sklyar, M. Boutros, W. Huber, EBImage - an R package for image processing with applications to cellular phenotypes. *Bioinformatics* **26**, 979-981 (2010).
3. R Core Team, R: A language and environment for statistical computing. *R Foundation for Statistical Computing, Vienna, Austria.* URL https://www.R-project.org/ (2020).
4. B. L. Sprague, F. Muller, R. L. Pego, P. M. Bungay, D. A. Stavreva, J. G. McNally, Analysis of binding at a single spatially localized cluster of binding sites by fluorescence recovery after photobleaching. *Biophys J* **91**, 1169-1191 (2006).
5. K. Soetaert, F. Meysman, Reactive transport in aquatic ecosystems: Rapid model prototyping in the open source software R (vol 32, pg 49, 2012). *Environ Modell Softw* **35**, 194-194 (2012).
6. J. J. Hopfield, Kinetic proofreading: a new mechanism for reducing errors in biosynthetic processes requiring high specificity. *Proc Natl Acad Sci U S A* **71**, 4135-4139 (1974).
7. R. Shelansky, H. Boeger, Nucleosomal proofreading of activator-promoter interactions. *Proc Natl Acad Sci U S A* **117**, 2456-2461 (2020).
8. T. Kurosu, B. M. Peterlin, VP16 and ubiquitin; binding of P-TEFb via its activation domain and ubiquitin facilitates elongation of transcription of target genes. *Curr Biol* **14**, 1112-1116 (2004).
9. L. R. Polstein, C. A. Gersbach, A light-inducible CRISPR-Cas9 system for control of endogenous gene activation. *Nat Chem Biol* **11**, 198-200 (2015).
10. A. Rademacher, F. Erdel, J. Trojanowski, S. Schumacher, K. Rippe, Real-time observation of light-controlled transcription in living cells. *J Cell Sci* **130**, 4213-4224 (2017).
11. I. B. Hilton, A. M. D'Ippolito, C. M. Vockley, P. I. Thakore, G. E. Crawford, T. E. Reddy, C. A. Gersbach, Epigenome editing by a CRISPR-Cas9-based acetyltransferase activates genes from promoters and enhancers. *Nat Biotechnol* **33**, 510-517 (2015).
12. J. H. Shrimp, C. Grose, S. R. T. Widmeyer, A. L. Thorpe, A. Jadhav, J. L. Meier, Chemical Control of a CRISPR-Cas9 Acetyltransferase. *ACS Chemical Biology* **13**, 455-460 (2018).
13. T. Jegou, I. Chung, G. Heuvelman, M. Wachsmuth, S. M. Gorisch, K. M. Greulich-Bode, P. Boukamp, P. Lichter, K. Rippe, Dynamics of telomeres and promyelocytic leukemia nuclear bodies in a telomerase-negative human cell line. *Mol Biol Cell* **20**, 2070-2082 (2009).
14. F. Erdel, A. Rademacher, R. Vlijm, J. Tunnermann, L. Frank, R. Weinmann, E. Schweigert, K. Yserentant, J. Hummert, C. Bauer, S. Schumacher, A. Al Alwash, C. Normand, D. P. Herten, J. Engelhardt, K. Rippe, Mouse Heterochromatin Adopts Digital Compaction States without Showing Hallmarks of HP1-Driven Liquid-Liquid Phase Separation. *Mol Cell* **78**, 236-249 e237 (2020).
15. L. Frank, R. Weinmann, F. Erdel, J. Trojanowski, K. Rippe, in *Enhancers and Promoters: Methods and Protocols, Methods in Molecular Biology,* T. Borggrefe, B. Daniele Giaimo, Eds. (Springer Nature, New York, 2021), pp. in press.
16. K. Gunther, M. Rust, J. Leers, T. Boettger, M. Scharfe, M. Jarek, M. Bartkuhn, R. Renkawitz, Differential roles for MBD2 and MBD3 at methylated CpG islands, active promoters and binding to exon sequences. *Nucleic Acids Res* **41**, 3010-3021 (2013).
17. T. Frahm, H. Hauser, M. Koster, IFN-type-I-mediated signaling is regulated by modulation of STAT2 nuclear export. *J Cell Sci* **119**, 1092-1104 (2006).
18. D. Bracha, M. T. Walls, M. T. Wei, L. Zhu, M. Kurian, J. L. Avalos, J. E. Toettcher, C. P. Brangwynne, Mapping Local and Global Liquid Phase Behavior in Living Cells Using Photo-Oligomerizable Seeds. *Cell* **175**, 1467-1480 e1413 (2018).
19. U. Rothbauer, K. Zolghadr, S. Muyldermans, A. Schepers, M. C. Cardoso, H.

Leonhardt, A versatile nanotrap for biochemical and functional studies with fluorescent fusion proteins. *Mol Cell Proteomics* **7**, 282-289 (2008).
20. I. U. Rafalska-Metcalf, S. L. Powers, L. M. Joo, G. LeRoy, S. M. Janicki, Single cell analysis of transcriptional activation dynamics. *PLoS One* **5**, e10272 (2010).
21. J. G. Zalatan, M. E. Lee, R. Almeida, L. A. Gilbert, E. H. Whitehead, M. La Russa, J. C. Tsai, J. S. Weissman, J. E. Dueber, L. S. Qi, W. A. Lim, Engineering complex synthetic transcriptional programs with CRISPR RNA scaffolds. *Cell* **160**, 339-350 (2015).